Hassan, M. M., Ismail, Z. S., Hashem, E. M., Ghannam, R. and Abdellatif, S. O. (2021) Investigating the tradeoff between transparency and efficiency in semitransparent bifacial mesosuperstructured solar cells for millimeter-scale applications. IEEE Journal of Photovoltaics, (doi: 10.1109/JPHOTOV.2021.3086443).

http://eprints.gla.ac.uk/243100/

Investigating the trade-off between transparency and efficiency in semi-transparent bifacial meso-superstructured solar cells for millimeter-scale applications

Minatallah M. Hassan, Zahraa S. Ismail, Elhussien M. Hashem, Rami Ghannam, Senior Member IEEE
and Sameh O. Abdellatif, Senior Member IEEE

Abstract-- **Thanks to recent advancements in nanofabrication and 3D packaging, typical Internet of Things (IoT) devices can now be wirelessly controlled using millimeter scale sensors known as Internet of Tiny Things (IoT²) devices. Since these low power devices may be exposed to low and indirect solar irradiation, we demonstrate a novel meso-superstructured solar cell (MSSC) that allows low flux light to be harvested from both its top and bottom sides. Our cell is based on either a dye-sensitized solar cell (DSSC) or a perovskite solar cell (PSC). The active layer in the proposed MSSCs was tuned to allow semi-transparent behavior. Moreover, we developed an experimentally validated model that enables optimization of the active layer thickness for different semi-transparent MSSC applications. In MSSCs, such optimization is necessary to balance the trade-off between transparency and efficiency for various active layer thicknesses. Fabricated DSSCs and PSCs cells were used to validate the simulation results. The fabricated DSSC achieved a harvesting ratio of 1:10 with a conversion efficiency of around 2% at one Sun. We demonstrate that the optimum thickness of the mesoporous TiO_2 active layer in DSSCs was 800 nm, enabling a maximum power density of 7 mW/cm².**

Index Terms—**Optoelectronic modeling, mesoporous TiO_2, semi-transparent solar cells, Efficiency, J-V measurements, Low power applications.**

I. INTRODUCTION

The rising demand for low cost, high-efficiency and environmental friendly solar cells led to the emergence of a range of "third-generation" photovoltaic technologies [1], which include Dye Synthesized Solar Cells (DSSCs) [2] and Perovskites Solar Cells (PSCs) [3]. Often, these solution processed solar cells are called meso-superstructured solar cells (MSSCs), as mentioned by Snaith et al. [4], as well as our previous work in [5, 6]. In both types of solar cells, TiO_2 plays an important role in their operation. For example, the TiO_2 layer in DSSC is an n-type semiconductor where the dye diffuses through its pours forming the main active layer [5]. However, TiO_2 in perovskite solar cells functionalizes as an efficient electron transport layer [3].

Despite the low (yet rising) conversion efficiencies of DSSCs (13% [7]) as well as PSCs (25% [8, 9]) in comparison to silicon based solar cells (27% [10]), the use of toxic chemicals and the complex fabrication process make third-generation PVs more favorable. Another key feature of these cells is their ability to harvest light from both sides (back and front), thus allowing light to be harvested from the Sun as well as indoor artificial lighting. This capability allows MSSCs to serve wearable applications that require low-flux light to be harvested from multiple directions as well as photovoltaic window applications [11-15]. In the literature, a double-sided solar cell with a harvesting ratio of 1:6 was demonstrated [16].. However, the J-V curve showed a high level of fluctuation and uncertainties, which can impact the harvesting ratio.

Principally, MSSCs can be tuned to show a semi-transparent performance that is typically required in photovoltaic window applications [14]. However, this tunability creates a direct trade-off between transparency and efficiency. Additionally, photonic nano-structures can be integrated to enhance low-light harvesting efficiency, reject UV radiations and for decorative purposes [17, 18]. From an experimental prospective, our previous work in [14] considered this trade-off and we introduced a new figure of merit called "TED" to evaluate the semi-transparent solar cell performance due to conversion efficiency, transparency and efficiency under diffused light. Theoretically, previous attempts [19-23] have been conducted to model the optical performance as well as the carrier transport behavior in MSSCs either using drift-diffusion model [22] or by integrating density function theory (DFT) models [23]. However, no special theoretical focus on the trade-off between transparency and efficiency has been highlighted in literature.

In this work, optoelectronic models have been developed, tested, validated, and integrated to describe the performance of semi-transparent MSSCs used in photovoltaic window

Minatallah M. Hassan is with Basic-science department, Faculty of Engineering and FabLab in the Center for Emerging Learning Technology (CELT), The British University in Egypt (BUE), Cairo, Egypt (e-mail: Minnatullah.Moustafa@bue.edu.eg)

Zahraa S. Ismail and Sameh O. Abdellatif is with Electrical Engineering department, Faculty of Engineering and FabLab, Centre for Emerging Learning Technologies (CELT), The British University in Egypt (BUE), Elshrouk City, Cairo, Egypt. (e-mail: Zahraa.Ismail@bue.edu.eg, sameh.osama@bue.edu.eg).

Elhussein M. Hashem is with FabLab, Centre for Emerging Learning Technologies (CELT), The British University in Egypt (BUE), Elshrouk City, Cairo, Egypt. (e-mail: elhusseinhashem93@gmail.com).

Rami Ghannam is with School of Engineering, University of Glasgow, UK (e-mail: Rami.Ghannam@glasgow.ac.uk).

Corresponding author: Sameh O. Abdellatif, e-mail: sameh.osama@bue.edu.eg Mailing address: Elshrouk city Cairo-Suez Road, 11387, Cairo, Egypt.

applications. The trade-off between transparency and efficiency is clearly studied with respect to the active layer thickness reaching an optimum compensation thickness for each technology. The theoretical results have been validated using both our fabricated segmented and complete solar cells as well as our reported data in [5, 6, 14, 24]. The observed captured power per unit area exceeded the threshold power needed in operating various internet of tiny things (IoT[2]) applications [25], which allows for the utilization of semi-transparent MSSCs in smart building-integrated photovoltaics (BIPV) [26].

The remainder of our article is organized as follows. In section II we describe our optoelectronic model in terms of an analytical optical model and numerical carrier transport simulation platform. Section III demonstrates the experimental recipes used for fabricating MSSCs as well as the characterization procedures. Finally, validation process and optimization are illustrated in the results section.

II. Optoelectronic Modelling

Chemical based solar cells could be mainly fabricated from the same structure; it is only a matter of preparing the layers and assembling them together. This can be seen in figure 1, as it shows a schematic diagram of two types of chemical based MSSCs, such as DSSC and PSC. They are categorized as MSSCs due to the dominating effect of the resizable mesoporous particles TiO_2 (mpp-TiO_2) layer. It is also important to note that the two proposed schematics support bifacial light harvesting and exhibit transparent properties. Figure 1-a shows the schematic of a DSSC, including two conductive glass electrodes, a blocking compact TiO_2 layer, a mpp-TiO_2 layer, dye, and electrolyte. The mpp-TiO_2 is responsible for separating charges, collecting electrons, and conducting ions. Its thickness is also the main parameter strongly influencing the transparency of the produced solar cell. Here, compact TiO_2 is used for blocking ion transportation and overcoming the loss of generated electrons [5].

The operation of such cells involves the following, when a photon hits the dye particles; an electron is released and injected into the conduction band of the mpp-TiO_2 layer leaving a hole behind. The electrolyte then helps the dye restore its original state after losing the electron due to the photon excitation. This happens by a process known as electron donation, where electrolytes are usually made up from a redox mediator material. Next, thin platinum (Pt) layer is used to help the cell conduct electricity better. Finally, the FTO coated glass electrodes create the full closed cycle for the charges to travel through it, creating a well-constructed DSSC.

In contrast, figure 1-b shows the schematic diagram of a PSC as FTO/TiO_2/$CsPbBr_3$/NiO/FTO structure. In this structure, a $CsPbBr_3$ perovskite layer, which is inserted between the electron transport material (ETM) and hole transport material (HTM) layers, is used as the light-absorbing material. Our motivation to use $CsPbBr_3$ was based on its compatibility with the sol-gel deposition technique and its semi-transparent capabilities, rather than its use for high efficiency solar cell applications. Two layers of TiO_2 (mesoporous and compact) were placed on the top of fluorine doped tin oxide (FTO) substrate to form the photo-anode. The TiO_2 layer is a well-known electron transporting layer (ETL) and its role is to transport electrons in the solar cell and serve as a hole blocking layer (HBL) to reduce charge recombination and

prevent electrode shorting [27]. Similarly, NiO functionalizes as a hole transporting layer [28]. An excited (electron-hole pair) is generated in the active layer due to absorption of light. These free holes and electrons must be collected by their corresponding electrodes in order to produce electric current before recombining (non-radiative or radiative) [27].

Our proposed optoelectronic model can be divided into two important parts. The first deals with the interaction of light with the various layers in our MSSC structure, whereas the second deals with carrier transport as a result of electron-hole pair generation. In the next sub-sections, we will describe the details of our modeling approach.
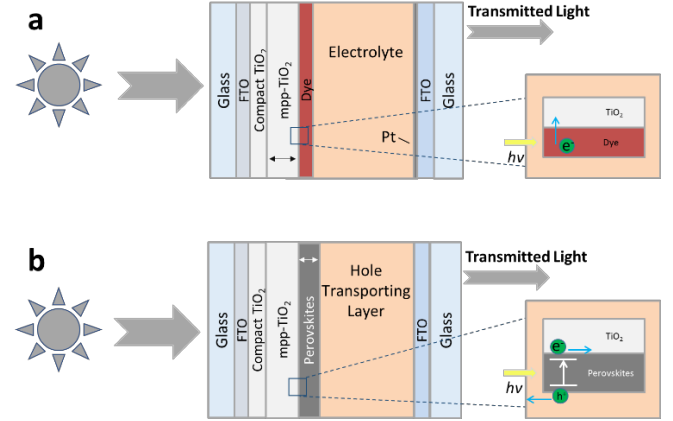

Figure 1: (a) Schematic of a DSSC with an illustration of the photon-induced electron transfer, (b) Schematic of a PSC with an illustration of the photon-induced electron-hole generation.

A. Optical modeling

Optical modelling is an essential process that should be carried out to be able to study the performance of solar cells. According to the literature, the optical modelling of new and emerging solar cells using analytical optics is a challenge. Herein, our optical modelling of electro-chemical solar cells was introduced as a simple cascaded series of thin films. The model was implemented and tested on DSSCs. However, it can be expanded to other MSSCs such as PSCs [29, 30], as well as other types of emerging solar cells including organic solar cells and quatum-dot based solar cells. The transmission, reflection and absorption of DSSCs with variable active layer thickness have been studied. The proposed model simply works by solving the transmission coefficient (t) and reflection coefficient (r) as following [31]:

$$t = \frac{2\gamma_o}{\gamma_o m_{11} + \gamma_o \gamma_s m_{12} + m_{21} + \gamma_s m_{22}} \quad (1)$$

$$r = \frac{\gamma_o m_{11} + \gamma_o \gamma_s m_{12} - m_{21} - \gamma_s m_{22}}{\gamma_o m_{11} + \gamma_o \gamma_s m_{12} + m_{21} + \gamma_s m_{22}} \quad (2)$$

giving that:

$$\gamma_o = \frac{n_{incident}}{120\pi} \quad (3)$$

$$\gamma_s = \frac{n_{substrate}}{120\pi} \quad (4)$$

$$m_{11} = \cos(k_o h); \quad m_{12} = \frac{I \sin(k_o h)}{\gamma_1};$$

$$m_{21} = i \sin(k_o h) \gamma_1 \text{ and } m_{22} = m_{11} \quad (5)$$

$$k_o = \frac{2\pi}{\lambda} \quad (6)$$

$$h_1 = h_{propagating\ medium} * n_{propagating\ medium} \quad (7)$$

Where:

$h_{propagating\ medium}$	the material's thickness
$n_{propagating\ medium}$	the material refractive index
$n_{incident}$	the refractive index of the in-going medium
$n_{substrate}$	the refractive index of the out-going medium
k_o	the propagation constant
λ	the propagating wavelength
$m_{11}, m_{12}, m_{21}, m_{22}$	the characterization matrix elements
γ_o	the normalized refractive index of the in-going medium
γ_s	the normalized refractive index of the out-going medium

In the current study, wavelength variation is from 200 nm to 1000 nm, which covers the UV-Vis-NIR region. Additionally, refractive indices considered in this model are represented as a complex dispersive/absorptive function in wavelength as described later in this paper. The light propagation analysis followed in the proposed tool is based on the layer arrangement of a simple DSSC (see figure 1-a).

To be able to use the proposed optical model correctly, a set of important data are needed to be acquired beforehand, these are core data that affect the obtained results drastically. Therefore, all important parameters have been acquired for each layer and tabulated in table 1. Each parameter has been either extracted or calculated, based on measured data from literature. It can be observed from the listed parameter in table 1 that both the electrolyte and the platinum layers have been neglected from the optical point of view. For the electrolyte medium as well as the platinum thin layer on the counter electrode, our recorded results have shown its full high transparency spectrum with respect to other scattering and absorbing layer in the arrangement. More details and spectral analysis for electrolyte can be addressed in Appendix A, figure A.1. Concerning the platinum layer, the ultra-thin layer, typically one to two nanometers, makes it possible to exclude any possible absorption within the layer (cf. Appendix A, figure A.2).

As mentioned earlier, the proposed optical model is not only exclusive for DSSCs in matter of fact it can be extended to describe other electrochemical solar cells such as PSCs, as far as the refractive index, dispersion and extinction are defined for each layer. The suggested model has been scripted using Matlab and can be accessed through: [32], also available in the Supplemented Materials.

B. Carrier transport modelling

A computer-based simulation software known as Solar Cell Capacitance Simulator (SCAPS-1D) was used to numerically simulate the output characteristics of solar cells. It was designed to find numerical solutions of a system of three coupled differential equations consisting of three basic semiconductor equations (the poisson, the electron continuity, and the hole continuity equations) [33]. SCAPS can describe a solar cell as a series of semiconductor layers and contacts with different optoelectronic properties as well as defect states of each interface and layer. SCAPS is capable of simulating the open circuit voltage (V_{oc}), the short circuit current density (J_{sc}), the fill factor (FF), and the overall power conversion efficiency (PCE) for the designed solar cell under study.

As previously mentioned, we are interested in investigating the influence of varying the absorber layer thickness on the performance of the PSCs and DSSCs. Table 2 shows the input simulation parameters needed for simulating the carrier transport in DSSC. The given parameters have been extracted from previous work [5, 34-36], There are other parameters that are not mentioned in the table such as thermal velocity and absorption coefficient which are set as 10^7 cm/s and 10^5 cm^{-1}, respectively. The defect type of the absorber layer is set as neutral (so that this defect leads to Shockley-Read-Hall recombination and not space charge) and the capture cross section of hole and electron are set as 1×10^{-15} cm^2. The characteristic energy is set as 0.1 eV, and energetic distribution is set as Gaussian.

TABLE 1
EXTRACTED OPTICAL PARAMETERS FOR DIFFERENT LAYERS OF DSSC.

……	Refractive Index	Thickness	Specification
Glass (BK7)	1.46 [37]	2.2 mm	None-dispersive with 8% reflection
FTO	2.14 (Calculated)	180-200 nm	None-dispersive 80% transmittance
Compact TiO$_2$	1.9 ± 0.005 [5]	264.0±1.5 nm [5]	Dispersive material
Mesoporous TiO$_2$+N719 Dye	1.62 ± 0.002 [5]	5-15 μm [5]	Dispersive material with scattering [38]
Iodide Electrolyte	1.4426 (Calculated)	30 μm	Assumption: Optical properties is neglected
Platinum	2.0847 [39]	1-2 nm	Assumption: Optical properties is neglected

As for the PSC, table 3 summarizes the input material parameters from in the literature [20, 28, 40, 41]. Two defect interfaces (CsPbBr$_3$/NiO and TiO$_2$/CsPbBr$_3$) were used for carrier recombination [28]. Table 4 summarises the defect parameters for each layer used in the simulation model [20, 28, 42]. Control variable method was implemented for parameter optimization. The hole density in the TiO$_2$ ($\approx 10^{13}$ cm^{-3}) is much lower than the electron density (10^{18} cm^{-3}). The same densities were used for the NiO layer ($\approx 10^{13}$ cm^{-3} for electrons and 10^{18} cm^{-3} for holes). This verifies the effectiveness of the transport layers.

SCAPS also treats some tunnelling mechanisms by implementing the model for interface transport as thermionic emission for both simulated models. The thermal velocity of the interface transport for electron and hole was in order of 10^7 cm s^{-1} [40]. The optical reflectance was set to zero at each interface and at the surface. Moreover, the operating temperature was set to 300 K and AM1.5 global irradiation conditions were used.

TABLE 2
Input parameters for the carrier transport modelling of DSSC [34-36].

Parameters	Pt	Electrolyte	Mesoporous TiO$_2$ + N719 Dye	Compact TiO$_2$
Thickness (μm)	0.080	30	4.260	0.2
Band-gap energy Eg (eV)	1.9	1.9	3.2	3.2
Electron affinity χ (eV)	3.650	3.7	4	3.9
Relative permittivity	3.700	3.790	2.624	1.798
Electron effective DOS N$_c$ (cm^{-3})	2×10^{20} (fitted)	$6.020 \times 10^{1'}$ (fitted)	2.4×10^{20} (fitted)	1×10^{15} (fitted)
Hole effective DOS N$_v$ (cm^{-3})	2×10^{20} (fitted)	$6.020 \times 10^{1'}$ (fitted)	2.5×10^{20} (fitted)	1×10^{15} (fitted)
Electron mobility μn (cm^2 V^{-1} s^{-1})	1×10^{-8}	1×10^{-1}	3	20
Hole mobility μp (cm^2 V^{-1} s^{-1})	1.28×10^{-5}	3×10^{-1}	3	10
Donor concentration N$_D$ (cm^{-3})	0	0	0	1×10^2
Acceptor concentration N$_A$ (cm^{-3})	1×10^6 (fitted)	1×10^5 (fitted)	0	10 (fitted)
Defect/trap density N$_t$ (cm^{-3})	-	-	6×10^{11} (fitted)	-

III. EXPERIMENTAL WORK

A. DSSC fabrication

To validate the optoelectronic modelling results, experimental data had to be acquired. Accordingly, the fabrication of MSSCs was essential. For DSSCs, the recipe mentioned in Appendix B table A.1 was used. The data presented in B shows the recipes for all the layers needed to fabricate the proposed DSSCs. After preparing all the layers beforehand as stated in B, the assembly stage begins. First, we start by depositing the compact TiO$_2$ layer on the FTO coated side of the electrode using a spin coater (500 rpm at the beginning for 10 s, followed by a 3000 rpm step for 60 s with constant acceleration of 1000 rpm/s as reported in [5]), then after annealing the sample a layer of the pre-prepared mpp-TiO$_2$ paste is deposited above the compact TiO$_2$ layer. The glass is then heated again until the paste dries out and becomes well attached to the substrate. Secondly, the cooled-out sample is submerged in the N719 pre-prepared dye. Once the sample is completely stained, it is time to close the cell using the counter electrode (catalyst coated electrode), leaving behind a space for the probes

to be connected, with the conductive sides facing each other. Then finally, the electrolyte is injected through the top and allowed to fill up the cell, producing a complete DSSC.

TABLE 3
Input parameters for the carrier transport modelling of PSC [20, 28, 40, 41], where N$_V$, N$_C$ are hole and electron effective density of states, respectively. N$_t$, N$_A$ and N$_D$ are trap density, shallow uniform acceptor density and shallow uniform donor density, respectively.

Parameters	FTO	ETM (TiO$_2$)	CsPbBr$_3$	HTM(NiO)
Thickness (nm)	300	480	350	245
Band-gap energy Eg (eV)	3.5	3.2	2.3	3.6
Electron affinity χ (eV)	4.5/4.8	4.2	3.6	1.8
Relative permittivity	10	9	6.5	11.75
N$_c$ (cm^{-3})	2×10^{18}	1×10^{18}	4.94×10^{17}	2×10^{18}
N$_v$ (cm^{-3})	1.8×10^{19}	1×10^{19}	8.47×10^{18}	2×10^{18}
Electron mobility μ$_n$ (cm^2 V^{-1} s^{-1})	100	0.05	4500	0.2
Hole mobility μ$_p$ (cm^2 V^{-1} s^{-1})	20	0.025	4500	0.2
Donor concentration N$_D$ (cm^{-3})	1×10^{20}	1×10^{18}	1×10^{15}	10^{13}
Acceptor concentration N$_A$ (cm^{-3})	0	10^{13}	0	1×10^{18}
Defect density N$_t$ (cm^{-3})	1×10^{15}	1×10^{15}	1.5×10^{12}	1×10^{15}

B. PSC fabrication

Perovskite materials are attracting plenty of attention in solar cell applications. However, further development of hybrid perovskite-based optoelectronic devices is limited by the intrinsic thermal instability of formamidinium (FA) and methylammonium (MA) based perovskite materials. Therefore, all-inorganic perovskites have recently been suggested as alternative materials for optoelectronic devices due to their interesting electronic properties and their higher chemical stability in comparison to the thermal degradation of hybrid perovskites. An example is cesium lead halide (CsPbX$_3$, X = Br, Cl, and I). In previous experimental works, solution process approach was used to prepare most of perovskites based optoelectronic devices, which would refer to the spin coating method and long-chain organic ligands [43-45].

The chemicals used in the synthesis are cesium bromide (CsBr), lead bromide (PbBr2), dimethyl form amide (DMF) and methanol. First, a glass substrate was cleaned by consecutive 20 minutes sonication in warm deionized water, isopropanol, and acetone. The Substrate was preserved with UV-ozone for 15 minutes, after drying under a nitrogen flow at atmosphere. Afterwards, the substrate was annealed at 75 °C before using [43].

Two-steps sequential deposition technique was used to prepare the CsPbBr$_3$ film. First of all, 0.03 grams of CsBr was dissolved in 2 mL of methanol and then heated in a sealed container for 10 minutes. Next, a solution of 0.367 grams of PbBr$_2$ and 1 mL of DMF were stirred on a hot plate at 75°C for 5 hours. Then the PbBr$_2$ layer was filtered using a 0.22 μm pore size PTFE

(Polytetrafluoroethylene) Membrane Filter and then used immediately. A spin-coater was used to deposit the PbBr$_2$ layer at 4000 rpm for 40 seconds on the cleaned preheated glass substrate, then it was left to dry out at 75°C for 30 minutes. After drying for 30 minutes, the substrate was immersed for 5 to 15 minutes in a heated (50°C) solution of 15 mg/mL of CsBr and then strengthened at 180°C on the hot plate directly [43]. The complete PSC fabrication recipe can be addressed in Appendix B Table A.2.

TABLE 4
Defect parameters of interfaces and absorber [20, 28, 42].

Parameters	CsPbBr$_3$	TiO$_2$/CsPbBr$_3$	CsPbBr$_3$/NiO
Defect type	Neutral	Neutral	Neutral
Capture cross section for electrons (cm^2)	2x10^{-15}	2x10^{-16}	2x10^{-14}
Capture cross section for holes (cm^2)	2x10^{-15}	2x10^{-16}	2x10^{-14}
Energetic distribution	Gaussian	Single	Single
Energy level with respect to Ev (eV)	0.500	0.650	0.650
Characteristic energy (eV)	0.1	0.1	0.1
Total density (cm^{-3})	1.5x10^{12}	1x10^{17}	1x10^{17}

C. Characterization

The morphological structures of the prepared nanoparticles were estimated by P Analytical X'PERT MPD diffractometer using (Cu [Kα$_1$/Kα]) radiation. The variation in the diffraction angle is from 10º to 90º while applying a step of 0.02º with integration time of three s/step was utilized. The morphologies of the samples were analysed using High resolution transmission electron microscopy (SEM JEOL 6340). This step was conducted to validate the apriority of fabrication procedure used (address Appendix B figure A.3)

In order to study and characterize the fabricated DSSCs, an important tool has been designed and implemented to aid the process of examination, characterization and interpretation. This tool is an LED-based solar simulator with an integrated NIR-UV-Vis spectrometer and Keithley 2401 current-voltage source meter [46].

For the solar simulator, LEDs types and colours were chosen on the basis of the AM 1.5G spectrum. After surveying the possible choices, high power LEDs were purchased from LUMILEDS in the following colours: Deep Red, Far Red, Royal Blue, Cool White, Infrared and Ultraviolet. Before arranging the array, each LED was tested on its own. The array was then constructed, while considering the 1D and 2D arrangement effect on the produced spectrum. The spectrum measurement was conducted using UV-Vis spectrometer. Every set of arrangement yielded a different spectrum; this is due to the concept of spectrum mixing. After a set of iterations, it was possible to reach an arrangement that exhibit only 15% mismatching factor with respect to the AM 1.5G and could reach up to 12% mismatching factor at a distance of 10 cm from the source (cf. Figure 5 in our previous work in [46]).. After each arrangement of the LED array, an Ocean Optics UV-Vis-NIR spectrometer was used for acquiring the produced spectrum and comparing it with that of the AM 1.5G in order to calculate the mismatching percentage.

To measure the transparency of the fabricated segmented solar cells and the complete cells, as well as measure the absorption of the dyes, a V-770 UV-Visible/NIR Spectrophotometer was used, where the wavelength from 190 nm to 2700 nm can be investigated. The measurement process was carried out by simply placing the sample in the device and setting the wavelength range, then the device sweeps the sample and displays the result on its compatible software.

IV. RESULTS AND DISCUSSION

A. Material optical parameters modeling

Based on the optical model presented in section II.A, the refractive index for the given constructing layer of MSSC is considered as an essential input for appropriate optical modeling. Hence, the dispersive as well as the extinction behavior of the dominating layer should be defined. Herein, we considered both comp-TiO$_2$ and mpp-TiO$_2$ layers as the dominating layer with respect to the absorption as well as the scattering performance.

For mpp-TiO$_2$, the extinction spectrum can be treated as two portions: the first where absorption dominates (below 400 nm) and the second where scattering showed the major impact (above 400 nm). In the absorption dominating region, a Lorentz-Drude (LD) fitting process is applied following the technique introduced in our previous work in [5, 24], while the scattering effect is modeled using the Mie scattering fitting model of mpp-TiO$_2$ [5]. The data of the Mie scattering model has been extracted and used in the optical model proposed in section II.A, where the porosity of the layer is attributed as the main factor affecting the scattering spectrum. Similarly, for the compact TiO$_2$ layer the same extracted LD fitting parameters have been used. The parameters used in the LD fitting of the porous and compact TiO$_2$ can be found in Appendix C. Figure 2 shows the two extinction spectra used for simulating the two main layers, the compact TiO$_2$ layer and the mpp-TiO$_2$ layer. The two layers exhibit both dispersive and extinction behavior, which were represented using the refractive indices. The simulated data recorded an acceptable matching with respect to the data in literature [5] with a root mean square error less than 3.8% for a given porosity.

B. MSSCs optical modeling

In order to validate our optical model that is proposed in section II.A, a set of simulations have been carried out based on either experimental data or data obtained from literature for segmented MSSCs. Figure 3 illustrates two set of data, one that represent the transmission of a simulated compact TiO$_2$ layer deposited on glass "Simulated compact TiO$_2$" and its validation with an experimental prepared sample "experimental compact TiO$_2$". While the other represent the transmission of a simulated mpp-TiO$_2$ layer deposited on glass and submerged in N719 dye "Simulated mpp-TiO$_2$+N719 dye" and its validation with an experimental prepared sample "experimental mpp-TiO$_2$+N719 dye". It is observed from the graph that a nearly perfect matching is obtained for both samples above 350 nm. However, a relatively higher mismatching is detected in the far UV region for the

compact sample. We attribute this to the fitting of the LD coefficients. The recorded mismatching is not impacting on the current study as far as it is outside the visible portion of spectrum where transparency is defined.

On the other hand, figure 4 demonstrates the simulation of two samples of mpp-TiO$_2$ layers and two fabricated DSSCs. Based on the data presented in [14], these samples were prepared using two mpp-TiO$_2$ layer thicknesses: 4.26 μm and 1.93 μm. To validate the data presented in figure 4, a root mean square mismatching error was introduced between the simulated data and the measurement provided in [14] at a wavelength of 700 nm, where an acceptable mismatching (below 5%) error was observed. It was observed that the mismatching error fluctuated with a variation in wavelength (maximum error detected at 630 nm). We attribute this fluctuation to the Mie scattering model we used to describe the extinction behavior of the mesoporous layer. While it is mathematically challenging to describe the extinction behavior of randomly arranged porous layers, the Mie scattering model was used, as reported as in the literature [5]. For a complete cell's spectra, other mismatching parameters need to be included, such as the parasitic absorption in the electrolyte layer. Moreover, the wavy nature of the simulated data with respect to the corresponding experimental data in [14] can be attributed to the Fabry-Perot oscillations associated with the characteristic matrix method used in the optical modelling.
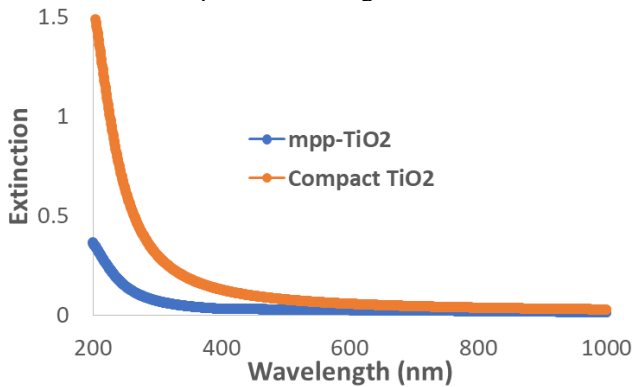
Figure 2: Extinction spectra of compact and mpp-TiO$_2$ layers. Extinction spectra are output from the proposed optical model using LD fitting.

For PSCs, following the recipe briefed in section III.B, CsPbBr$_3$ was deposited on BK7 glass using spin coater. The UV-Vis-NIR spectrum measurement is presented in figure 5. The same optical simulation model described above is utilized to describe the perovskite thin film with assuming the absence of any volume scattering mechanisms and extinction is limited to absorption. Again, the simulation results show perfect agreement measured data, with less than 2% error. It is worth to mention that CsPbBr$_3$ is chosen due to its simple deposition procedure as well as chemical availability in local market. However, the presented optical model can be easily extended to other CsPbX$_3$ as well as various perovskite materials.
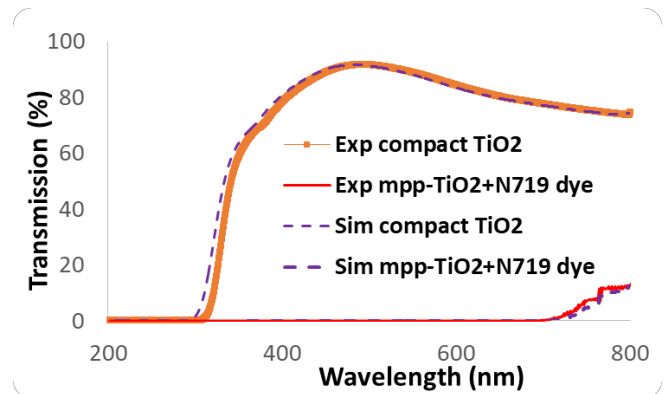
Figure 3: Transmission spectra for segmented DSSCs, experimental measurements and simulation data.
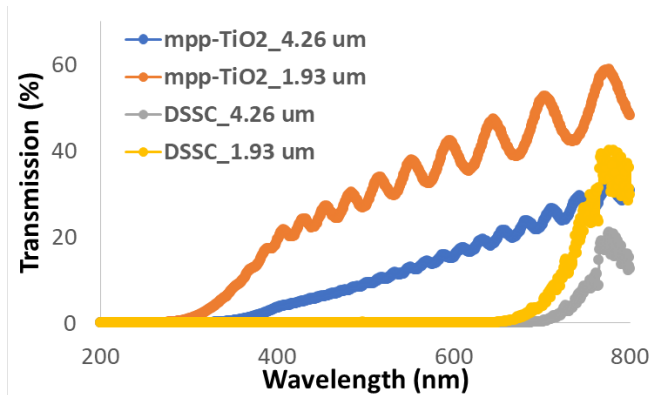
Figure 4: Simulation transmission spectra for segmented and complete DSSCs based on the active layer thickness and experimental data given in [14].
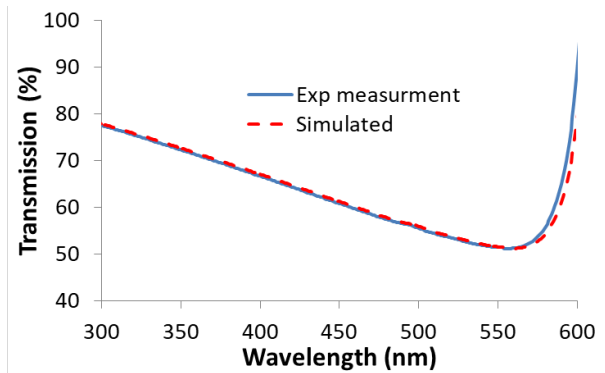
Figure 5: Transmission spectra for segmented PSC, experimental measurements and simulation data.

C. Carrier transport modeling results

In the SACPS device model simulation, the photocurrent density-voltage (J-V) performance of the simulated DSSC at absorber thickness 4.260 μm with the parameters mentioned in section II.B under AM1.5 sunlight illumination (100 mW/cm^2) was simulated (see figure 6). The simulation result is considered to be within the acceptable ranges as reported in [14], which can be used to validate the accuracy of the simulation model presented in this study. The main output parameters; open-circuit voltage (V$_{oc}$), short-circuit current (J$_{sc}$), fill factor (FF) and the power conversion efficiency (PCE) for the device at absorber thickness 4.260 μm were attained and compared with the real experimental measurement data reported in literature [14] as listed in table 5. The observed mismatching error for the open-circuit voltage,

short circuit current, power conversion efficiency, and fill factor is 1.6%, 3.56%, 4.13%, and 0.83%, respectively.

Additionally, another (J-V) characteristic curve was simulated for a fabricated DSSC using the recipe mentioned in III.A with active area of 5 cm² (cf. Figure 6). A modified model with updated input parameters has been used. The compact TiO_2 layer thickness was taken to be 0.6 μm. As for the active layer, the thickness is 10 μm. The simulation result is considered to be within the acceptable ranges as compared with the experimentally characterized DSSC, with mismatching percentages of 1.14% and 2% in short-circuit current and open circuit voltage, respectively. It can be observed that both cells (DSSC in literature [14] and DSSC characterized in figure 6) have different J-V behaviour, especially for higher voltages near the open circuit voltage. We attribute this to the parasitic resistance associated with each measurement setup. Herein, we utilize our previously published parasitic resistance determination algorithm to estimate such resistance per experimental measured J-V data [41, 47].
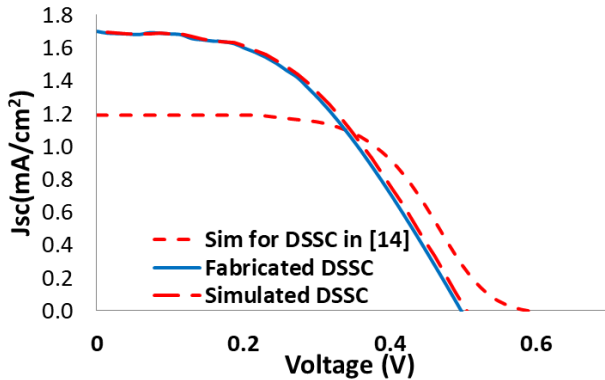
Figure 6: Simulated J-V characteristic curve for a DSSC at absorber thickness of 4.260 μm fabricated in [14] and experimentally fabricated and characterized DSSC following the recipe in section III.A with its associated simulation data.

TABLE 5

Photovoltaic parameters obtained from simulation compared to experimental data in [14].

Parameters	Simulation	Experimental
V_{oc} (V)	0.605	0.615
J_{sc} (mA/cm²)	1.194	1.153
FF (%)	60.1	60.6
PCE (%)	2.09	2.18

D. Semi-transport MSSCs optimization

The photoconductive layers of DSSC and PSC are considered as a decisive element in absorbing light and collecting charge. Therefore, the thickness of the active/absorber layer has a remarkable influence on the performance of the cells. In this simulation work, the thickness of the absorber layer is varied from 40 nm to 4 μm seeking for an optimum thickness in the efficiency transparency trade-off. The main target of the implemented optical model is to be able to study the trade-off between transparency and efficiency which is correlated with absorption. Principally, as the thickness of the active layer increases, absorption increases while transmission decreases. This can be easily noticed in figure 7, where it demonstrates a series of simulations of a complete DSSC with mpp-TiO_2 layer varying from 40 nm to 4 μm with utilizing our proposed optical model .

The photocurrent density-voltage (J-V) performances of the simulated PSC and DSSC at different thickness of the absorber film under AM1.5 sunlight illumination (100 mW/cm²) are shown in figures 8 and 9, respectively. The basic device performance parameters (J_{sc}, V_{oc}, FF and PCE) of the simulated DSSC and PSC were obtained and examined as a function of absorber thickness as listed in Appendix D.

As for PSC simulated model, it is obvious that as the thickness increases, the PCE slowly increases up to 400 nm with a maximum value of 3.91% and then slowly decreases. The increase of efficiency represents the production of new charge carriers and increase of optical density. This happens due to a higher spectral sensitivity of the absorber layer ($CsPbBr_3$) in the green region of the solar spectrum [28]. The slow decrease of PCE represents the increase of the recombination and less extraction rate of hole and electron pairs. As the thickness exceeds 400 nm, there will be a mismatch between the absorption depth of the absorber layer, and the carrier diffusion length, due to the recombination of the carriers before reaching the electrodes.

It is clear that increasing the thickness of the perovskite layer, increases the absorption of the light and thus increases J_{sc}. The J_{sc} then slowly saturates to 6.319 mA/cm² at approximately 800 nm to 900 nm thickness, and then decreases slightly when the absorber thickness exceeds 900 nm. This saturation is due to the increase of spectral response at the longer wavelength of illumination by increasing the absorber thickness. For absorbers greater than 800 nm, the current density decreases less because of reduction of the electric field in the absorber layer. Moreover, increasing the thickness of the perovskite layer up to 400 nm leads to a higher V_{oc} which remains constant and then decreases at 800 nm. This is due to the increase of series resistance and charge recombination [41, 47]. All simulated data are tabled in Appendix D.

On the other hand, a quick drop in the FF is observed, as it is strongly affected by electric field. By reducing the thickness of absorber layer, the depletion layer becomes very close to the back electrode and more electron charges will be captured by the back electrode for recombination. This means that the electric field in the active layer decreases while increasing the forward bias. It leads to a decrease in collection of charge carriers, which was assisted by the electric field. Thus, the absorber quality is bad for collection of current, leading to the drop in FF and efficiency with increasing the thickness. Thus, the maximum PCE of 3.91% with a V_{oc} of 1.126 V, J_{sc} of 5.669 mA/cm², and FF of 61.26% was obtained for the cell with an optimum thickness of 400 nm, which is the optimum value for a high efficiency device.

In a thin DSSC absorber (cf. figure 9), the charge carrier diffusion length is larger than the absorber thickness; most of the excess charge carriers are able to transfer and reach their corresponding electrodes in order to generate power. Therefore, increasing the thickness causes more light absorption of photons and more excess charge carrier concentration, which leads to higher values of J_{sc} (see Figure 9). Though, if the thickness is greater than the light diffusion depth, the photo-generation will reach a limit.
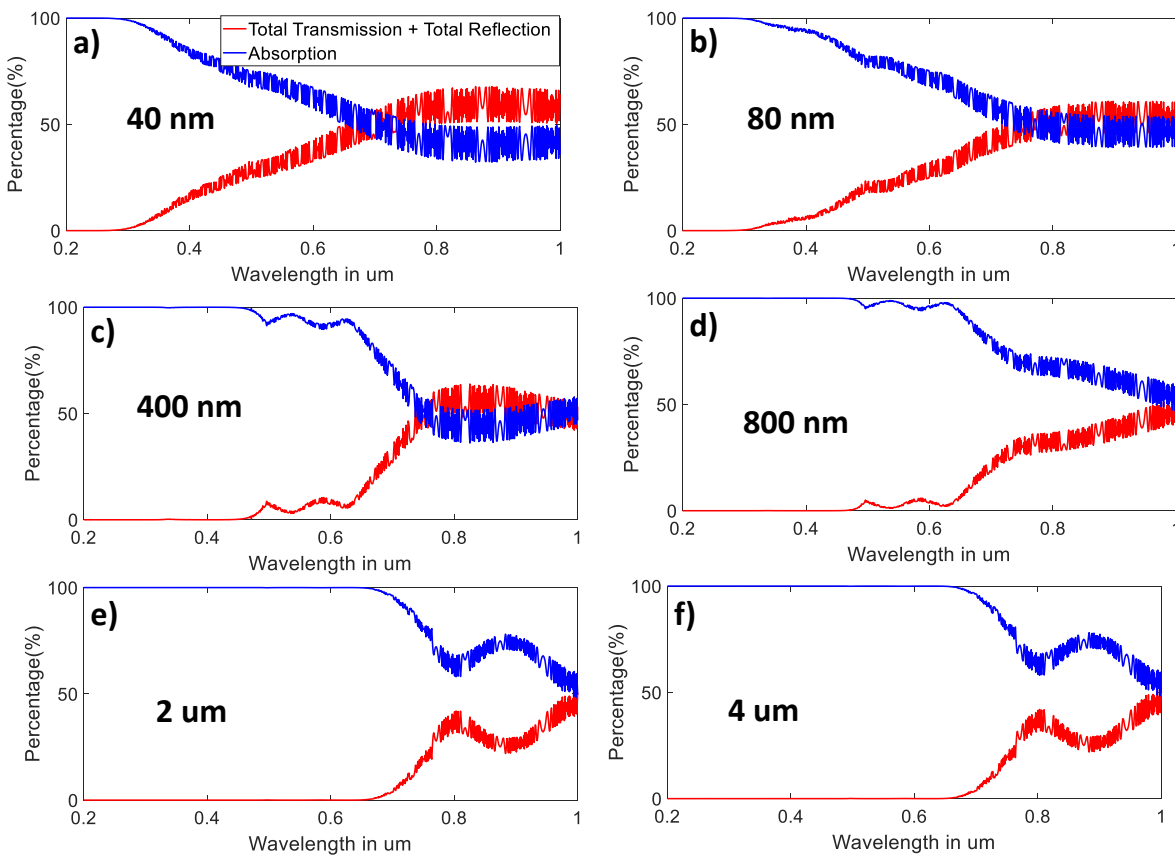
Figure 7: Optical modelling for the variation of the active layer thickness in DSSCs, absorption (blue) and total transmission and reflection (red) spectra.

As observed, V_{oc} increases to an optimal value of 0.6053 V at 4.260 μm thickness and then decreases strongly. In the increasing stage of V_{oc}, electron-hole recombination is lower with a thinner absorber layer and stays at a low magnitude, thus providing a low probability of carrier recombination, leading to a strong increase in V_{oc}. On the other hand, in the decreasing stage of V_{oc}, thicker absorber layer elevates to higher states and provide higher probability to carriers' recombination, leading to a strong decrease in V_{oc}. Additionally, the FF continues to drop from 69.99% to 60.9% with the absorber thickness varying from 40 to 4000 nm as FF is considered as the internal power depletion. In thicker absorber layer, the internal power depletion increases and causes a drop in FF.

The power conversion efficiency is mainly depends on two factors, carrier transport and photon absorption. Carrier transport is the challenge for thick absorber layer and photon absorption is the challenge for thin absorber layer. It can be derived that there is an optimal absorber thickness (4.260 μm) corresponding to higher efficiency. As a result, once the absorber thickness exceeds the optimal value, the probability for recombination starts to increase due to traps and excess charge carriers. Thus, the maximum PCE of 2.09% with a V_{oc} of 0.605 V, J_{sc} of 1.194 mA/cm^2, and FF of 60.1% was obtained for the cell with active layer thickness of 4.260 μm. All simulated data are provided in Appendix E.

Finally, results showing the overall DSSC conversion efficiency and cell transparency versus thickness are presented in figure 10. For the demonstrated data, the transparency was defined as the average transmission in the visible region. All transmission spectra can be found in Appendix E. Our simulation results can be used to determine an optimum point for the trade-off between transparency and efficiency in MSSCs, DSSC in particular for figure 10. Here, 800 nm was found to be the optimum thickness for achieving an average visible transparency of 19% and a conversion efficiency of 1.97% (the intersection point in figure 10). Consequently, this data was used for fabricating an optimized DSSC with bifacial energy harvesting capabilities and a harvesting ratio of 1:10. The cell's I-V curve is shown in figure 11. Herein, an equally weighted optimization approach was adopted between cell transparency and PCE. However, this weighting approach can vary depending on the application and its associated constrains (TED example in [14]). For example, in electrical vehicle technology, window transparency is obviously a critical parameter for driving and safety reasons. Therefore, transparency is equally as important as efficiency. On the other hand, in BIPV applications an unweighted optimization that is biased towards higher efficiency may be necessary.

Considering the low conversion efficiency of our proposed cells in comparison to those reported in the literature, we believe that these semi-transparent MSSCs are better suited to PV window applications, rather than wearable energy harvesting applications where area is constrained. keeping in mind the effectiveness of the proposed cell in harvesting diffused light as reported in our previous work [14]. In such context, the total power conversion efficiency of semi-transparent MSSCs is lower than the standard solar cells in the literature. While considering low diffused light intensity (below 20 mW/cm^2 with incident

angle greater than 45º), the diffused light conversion efficiency jumps to 3.5%). Accordingly, the proposed cell can harvest nearly 7 mW per unit area for one Sun condition, which matches the targeted IoT[2] applications [25].
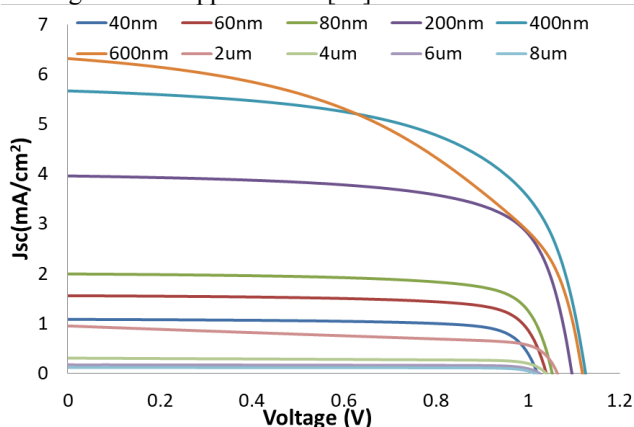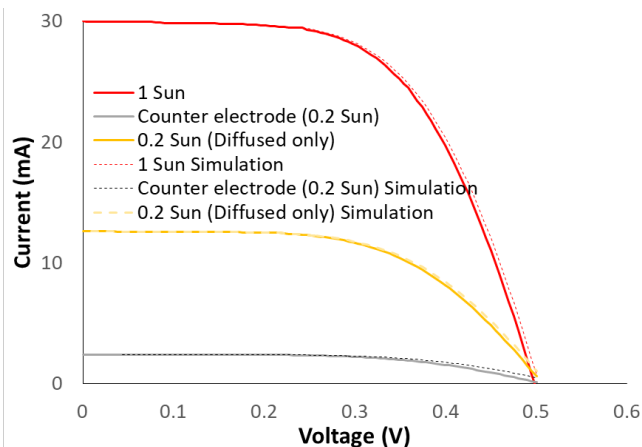

Figure 8: Current density vs. voltage characteristic of PSCs at different thickness of the CsPbCl$_3$ perovskite film.
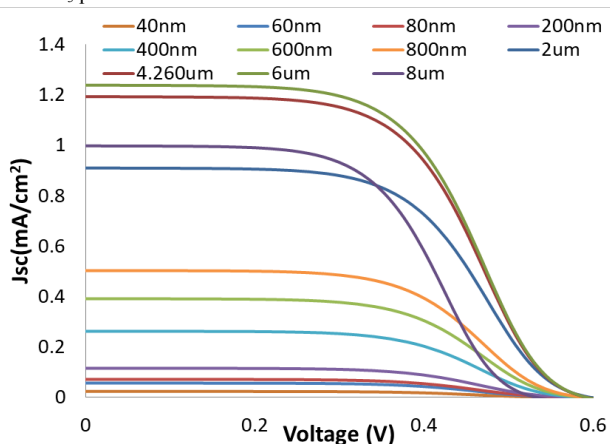
Figure 9: Current density vs. voltage characteristic of DSSCs at different thickness of the absorber film.
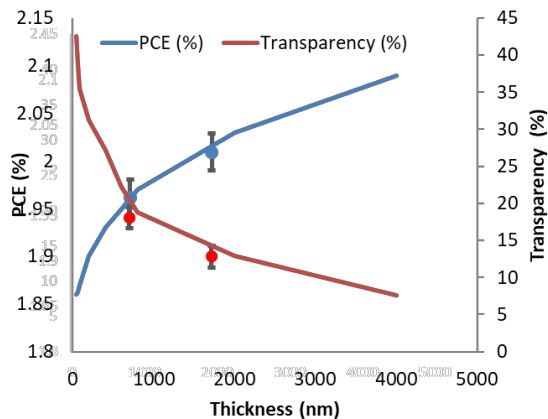
Figure 10: Transparency and efficiency variation with active layer thickness in DSSCs. Our simulation results show the optimum trade-off between transparency and efficiency. Experientially fabricated cells are indicated as scattered points with associated error bars.

Figure 11: Current vs. voltage characteristic of fabricated and simulated optimum 800 nm active layer DSSC under 1 Sun, 0.2 Sun and illuminated from both electrodes (bifacial).

V. CONCLUSIONS

Herein, we introduced an optoelectronic model to simulate the trade-off between transparency and efficiency in third generation PV cells, especially those with a mesoporous TiO$_2$ layer. The model showed good agreement with our fabricated and characterized cells as well as those reported in the literature. The proposed optoelectronic model can be extended to cover other organic/inorganic solar cells and further work is necessary to confirm this agreement. An 800 nm active layer DSSC was found to be optimum for semi-transparent applications, especially for ultra-low power IoT[2] applications. An overal harvested power of 7 mW/cm^2 was captured with 3.5% diffused light effeciency and nearly 2% direct light conversion effeciency. The proposed model can be expanded to include both inorganic and all organic PSCs, while considering this as a future extension to the current proposed model. We therefore conclude that new semi-transparent third generation solar cells have a sustainable market share in applications where opaque Si based solar cells can not fit.

VI. APPENDIX:

A. Electrolyte and platinum thin film transparency in DSSCs

In this section, the optical impact of both the electrolyte as well as the platinum coating on the counter electrode for DSSCs has been addressed. It can be observed for the spectrum in figure A.1 that the electrode behaviors a fully transparent behavior in the wavelength region of interest. Similarly, by comparing the FTO coated glass spectra with and without one to two nano-meters platinum coating, nearly matched spectra are detected (cf. figure A.2). Accordingly, we can neglect the optical influence of both layers in the proposed optical model.

B. The Complete recipe for MSSCs fabrication

In this section, we addressed a step-by-step recipes and fabrication procedures for both DSSC and CsPbBr$_3$ PSC in tables A.1 and A.2. Additionally, the SEM measuremnts along with the XRD analysis for the mesoprous TiO$_2$ layer is demonstrated in figure A.3a, b and c respectively. The demonstrated data approves the succsestion in the layer formulation.
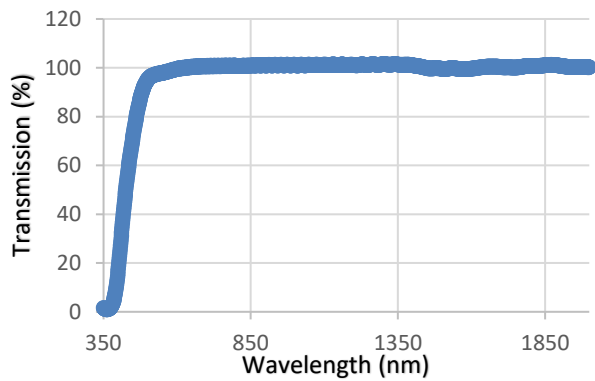
Figure A.1: Transmission spectrum for the Electrolyte layer based on the recipe described in the main text with considering glass substrate as a reference.

4
5
6
7
8
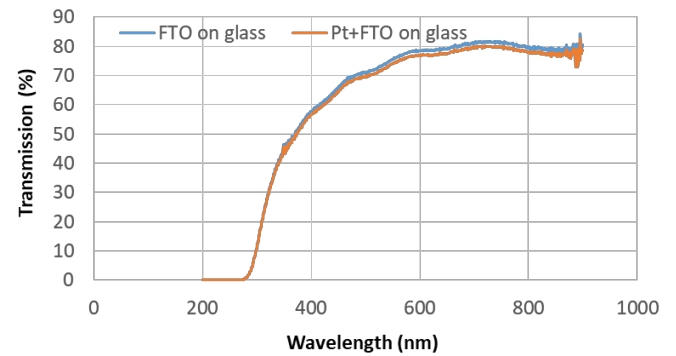
Figure A.2: Transmission spectra for FTO coated glass with and with platinum thin film with considering air as a reference.

9

TABLE A.1

Recipe and preparation of each layer for DSSCs.

Step No.	Step name	Needed Chemicals and Equipment	Description
1	Dye solution	Pre-prepared	N/A
2	Ethylene-glycol & Acetonitrile-based electrolyte	1. 0.24 g of I_2 2. 5 mL of Ethylene-glycol 3. 20 mL of Acetonitrile 4. 2.49 g of KI	1. Add 0.24 g I_2 along with 2.49 g KI to 5 ml Ethylene-glycol. 2. Add to the mixture 20 mL of Acetonitrile. 3. Mix on magnetic stirrer for 30 minutes until the solution is homogenous.
4	Triton-X based TiO_2 Paste for mesoporous layer	1. 2.5 g of TiO_2 powder 2. 3 mL Triton-X polymer 3. 0.75 ml iso-propanol	1. Add 2.5 g of TiO_2 powder with 3 mL Triton-X polymer. 2. Pestle till the mixture get homogenous. 3. Using a micro pipet add 0.75 ml of iso-propanol to the mixture and pestle again.
5	Compact TiO_2 layer	1. 170 mL of isopropanol 2. 12 mL of titanium iso-propoxide 3. 0.4 mL of 2MHCL	1. Add isopropanol and titanium iso-propoxide while stirring. 2. Drop by drop add 2M of HCl. 3. Stir using magnetic stirrer for over an hour. 4. Store in a dark place.
6	Graphite on counter electrode	1. Pencil	1. To prepare the counter electrode a thin layer of graphite was traced on the FTO side of the counter electrode.

32
33
34
35
36
37
38

TABLE A.2
Recipe and preparation of each layer for PSCs

Step No.	Step name	Description
1	Cleaning ITO transparent conducting substrates	ITO transparent conducting substrates were cleaned by sequential 20 min sonication in warm deionized water, acetone, and isopropanol.
2	Drying the substrates	After drying under a nitrogen flow at atmosphere, substrates were treated with UV-ozone for 15 min.
3	Treating the substrates with UV-ozone	Substrates were treated with UV-ozone for 15 min.
4	Annealing the substrate	Then annealed at 75 °C before using.
5	Preparing the CsPbBr₃ films by a 2-step sequential deposition technique	• Firstly, 30 mg CsBr was dissolved in 2 mL methanol. • Then was heated for 10 min in sealed container. • Subsequently, 367 mg PbBr₂ in 1 mL DMF was stirred on a hot plate at 75 °C for 5 h. • Then was filtered by using a 0.22 μm pore size PTFE filter and immediately for using. • The PbBr₂ layer was spin-coated at 4000 rpm for 40s on this well cleaned preheated (75 °C) ITO. • Then dried at 75 °C for 30 min

C. LD fitting parameters for TiO2 layers

TABLE A.3
LD fitting model parameters.

Parameter	Value
λ	From 200 to 1000 (nm)
ϵ_{ideal}	3.23352

D. Simulated parameter for MSSCs under varying active layer thickness

TABLE A.4
Photovoltaic performance of PSCs with different thicknesses of a perovskite layer at 100 mW/cm² and AM 1.5 simulated solar light.

	40nm	60nm	80nm	200nm	400nm	600nm	800nm	2μm	4μm
J_{sc}(mA/cm²)	1.087	1.563	1.999	3.964	5.669	6.319	6.213	0.9563	0.311
V_{oc} (V)	1.021	1.040	1.053	1.096	1.126	1.119	1.103	1.06	1.040
FF (%)	76.24	75.17	74.24	69.93	61.26	49.17	36.06	59.59	75.99
PCE (%)	0.85	1.22	1.56	3.04	3.91	3.48	2.47	0.61	0.25

TABLE A.5
Photovoltaic performance of DSSCs with different thicknesses of an active layer at 100 mW/cm² and AM 1.5 simulated solar light.

	40nm	60nm	80nm	200nm	400nm	600nm	800nm	2μm	4.260μm
J_{sc}(mA/cm²)	0.024	0.057	0.072	0.116	0.263	0.392	0.504	0.911	1.194
V_{oc} (V)	0.590	0.591	0.591	0.593	0.595	0.597	0.5986	0.605	0.6053
FF (%)	67.07	66.4	66.28	66.01	65.82	65.43	65.14	62.98	60.1
PCE (%)	1.86	1.863	1.87	1.90	1.93	1.95	1.97	2.03	2.09

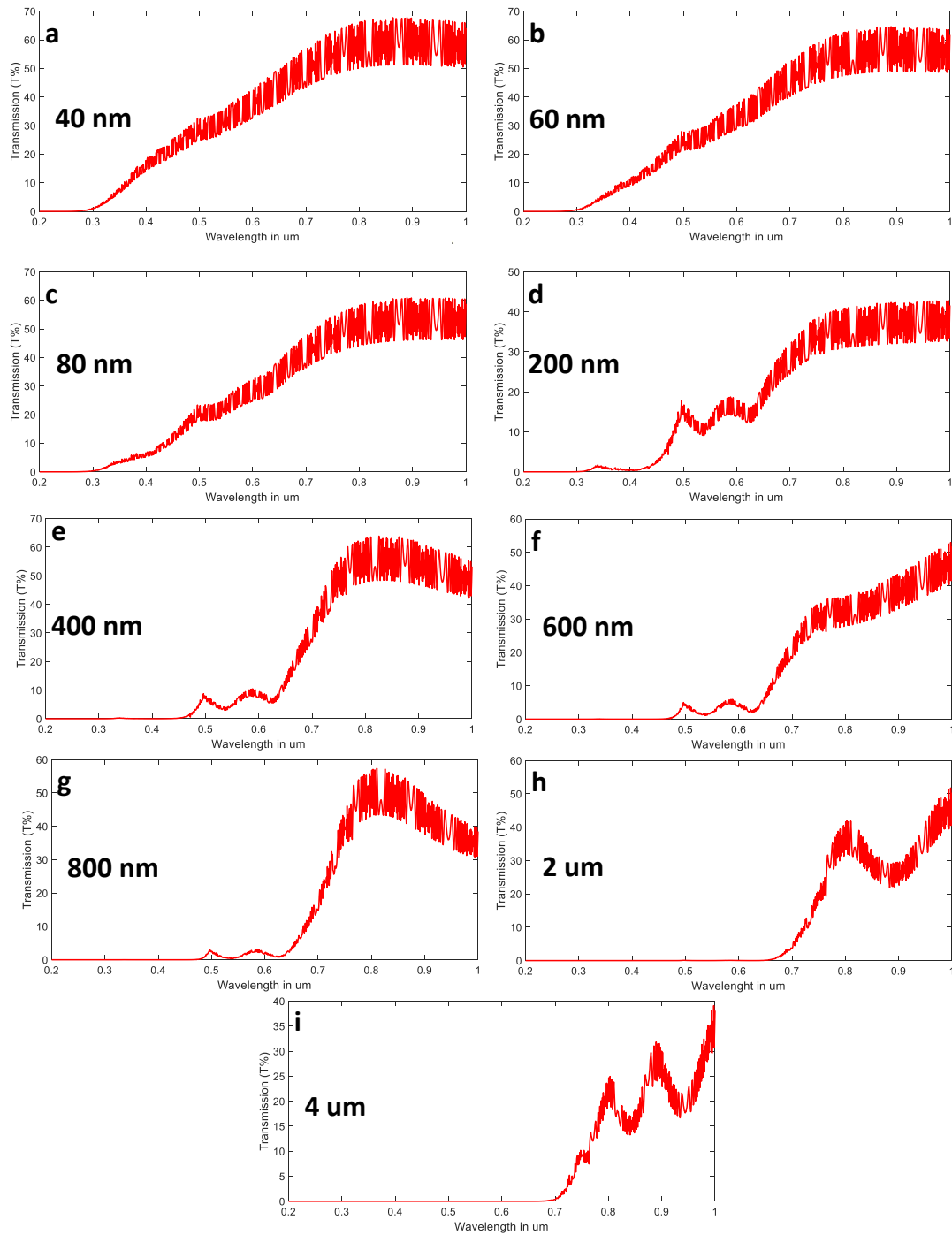*E. Simulated transmission spectra for DSSC under various active layer thickness*

Figure A.4: Simulated transmission spectrum for DSSCs under various active layer thicknesses from 40 nm to 4 μm.

VIII. REFERENCES

[1] M. A. Green, "Third generation photovoltaics: solar cells for 2020 and beyond," *Physica E: Low-dimensional Systems and Nanostructures,* vol. 14, no. 1-2, pp. 65-70, 2002.

[2] C.-P. Lee, C.-A. Lin, T.-C. Wei, M.-L. Tsai, Y. Meng, C.-T. Li, K.-C. Ho, C.-I. Wu, S.-P. Lau, and J.-H. He, "Economical low-light photovoltaics by using the Pt-free dye-sensitized solar cell with graphene dot/PEDOT:PSS counter electrodes," *Nano Energy,* vol. 18, pp. 109-117, 2015/11/01/, 2015.

[3] A. K. Chilvery, A. K. Batra, B. Yang, K. Xiao, P. Guggilla, M. D. Aggarwal, R. Surabhi, R. B. Lal, J. R. Currie, and B. G. Penn, "Perovskites: transforming photovoltaics, a mini-review< xref ref-type=," *Journal of Photonics for Energy,* vol. 5, no. 1, pp. 057402, 2015.

[4] M. M. Lee, J. Teuscher, T. Miyasaka, T. N. Murakami, and H. J. Snaith, "Efficient Hybrid Solar Cells Based on Meso-Superstructured Organometal Halide Perovskites," *Science,* vol. 338, no. 6107, pp. 643, 2012.

[5] S. Abdellatif, P. Sharifi, K. Kirah, R. Ghannam, A. Khalil, D. Erni, and F. Marlow, "Refractive index and scattering of porous TiO2 films," *Microporous and Mesoporous Materials,* vol. 264, pp. 84-91, 2018.

[6] S. Abdellatif, S. Josten, P. Sharifi, K. Kirah, R. Ghannam, A. Khalil, D. Erni, and F. Marlow, "Optical investigation of porous TiO2 in mesostructured solar cells." p. 105260A.

[7] S. Umale, V. Sudhakar, S. M. Sontakke, K. Krishnamoorthy, and A. B. Pandit, "Improved efficiency of DSSC using combustion synthesized TiO2," *Materials Research Bulletin,* vol. 109, pp. 222-226, 2019.

[8] T. Zhou, M. Wang, Z. Zang, and L. Fang, "Stable Dynamics Performance and High Efficiency of ABX3-Type Super-Alkali Perovskites First Obtained by Introducing H5O2 Cation," *Advanced Energy Materials*, pp. 1900664, 2019.

[9] C. M. Wolff, L. Canil, C. Rehermann, N. Ngoc Linh, F. Zu, M. Ralaiarisoa, P. Caprioglio, L. Fiedler, M. Stolterfoht, and S. Kogikoski Jr, "Perfluorinated Self-Assembled Monolayers Enhance the Stability and Efficiency of Inverted Perovskite Solar Cells," *ACS nano,* vol. 14, no. 2, pp. 1445-1456, 2020.

[10] M. Keevers, and M. Green, "Efficiency improvements of silicon solar cells by the impurity photovoltaic effect," *Journal of Applied Physics,* vol. 75, no. 8, pp. 4022-4031, 1994.

[11] W. Wang, Q. Zhao, H. Li, H. Wu, D. Zou, and D. Yu, "Transparent, double-sided, ITO-free, flexible dye-sensitized solar cells based on metal wire/ZnO nanowire arrays," *Advanced Functional Materials,* vol. 22, no. 13, pp. 2775-2782, 2012.

[12] W. Guo, X. Xue, S. Wang, C. Lin, and Z. L. Wang, "An integrated power pack of dye-sensitized solar cell and Li battery based on double-sided TiO2 nanotube arrays," *Nano letters,* vol. 12, no. 5, pp. 2520-2523, 2012.

[13] B. Aljafari, M. K. Ram, and A. Takshi, "Integrated electrochemical energy storage and photovoltaic device with a gel electrolyte." p. 1091318.

[14] S. O. Abdellatif, S. Josten, A. S. G. Khalil, D. Erni, and F. Marlow, "Transparency and Diffused Light Efficiency of Dye-Sensitized Solar Cells: Tuning and a New Figure of Merit," *IEEE Journal of Photovoltaics*, pp. 1-9, 2020.

[15] M.-E. Yeoh, and K.-Y. Chan, "A Review on Semitransparent Solar Cells for Real-Life Applications Based on Dye-Sensitized Technology," *IEEE Journal of Photovoltaics,* vol. 11, no. 2, pp. 354-361, 2021.

[16] G. Varnekar, "Integrated Tandem Dye Sensitized Solar Cell (DSSC)-Lithium Ion Battery," 2016.

[17] E. M. Hashem, M. A. Hamza, A. N. El-Shazly, M. F. Sanad, M. M. Hassan, and S. O. Abdellatif, "Investigating the UV absorption capabilities in novel Ag@RGO/ZnO ternary nanocomposite for optoelectronic devices," *Nanotechnology,* vol. 32, no. 8, pp. 085701, 2020/12/02, 2020.

[18] S. O. Abdellatif, K. Kirah, D. Erni, and F. Marlow, "Modeling disorder in two-dimensional colloidal crystals based on electron microscope measurements," *Applied Optics,* vol. 59, no. 33, pp. 10432-10440, 2020/11/20, 2020.

[19] P. Bhatt, M. Kumar, P. C. Kant, M. K. Pandey, and B. Tripathi, "Optoelectronic modelling of perovskite solar cells under humid conditions and their correlation with power losses to quantify material degradation," *Organic Electronics,* vol. 39, pp. 258-266, 2016.

[20] S. Z. Haider, H. Anwar, and M. Wang, "A comprehensive device modelling of perovskite solar cell with inorganic copper iodide as hole transport material," *Semiconductor Science and Technology,* vol. 33, no. 3, pp. 035001, 2018.

[21] K. Spiliotis, J. E. Gonçalves, D. Saelens, K. Baert, and J. Driesen, "Electrical system architectures for building-integrated photovoltaics: A comparative analysis using a modelling framework in Modelica," *Applied Energy,* vol. 261, pp. 114247, 2020.

[22] A. Riquelme, L. J. Bennett, N. E. Courtier, M. J. Wolf, L. Contreras-Bernal, A. Walker, G. Richardson, and J. A. Anta, "Deducing the key physical properties of a perovskite solar cell from its impedance response: insights from drift-diffusion modelling," *arXiv preprint arXiv:2003.07386*, 2020.

[23] G. Deogratias, N. Seriani, T. Pogrebnaya, and A. Pogrebnoi, "Tuning optoelectronic properties of triphenylamine based dyes through variation of pi-conjugated units and anchoring groups: A DFT/TD-DFT investigation," *Journal of Molecular Graphics and Modelling,* vol. 94, pp. 107480, 2020.

[24] S. Abdellatif, R. Ghannam, and A. Khalil, "Simulating the dispersive behavior of semiconductors using the Lorentzian–Drude model for photovoltaic devices," *Applied optics,* vol. 53, no. 15, pp. 3294-3300, 2014.

[25] S. Oh, D. Blaauw, and D. Sylvester, "The Internet of Tiny Things: Recent Advances of Millimeter-Scale Computing," *IEEE Design & Test,* vol. 36, no. 2, pp. 65-72, 2019.

[26] E. van der Poel, W. van Sark, Y. Aartsma, E. Teunissen, I. van Straten, and A. de Vries, "Steps Towards an Optimal Building-Integrated Photovoltaics (BIPV) Value Chain in the Netherlands, Sustainability in Energy and Buildings," *Sustainability in Energy and Buildings 2019*, pp. 409, 2020.

[27] Z. Song, S. C. Watthage, A. B. Phillips, and M. J. Heben, "Pathways toward high-performance perovskite solar cells: review of recent advances in organo-metal halide perovskites for photovoltaic applications," *Journal of Photonics for Energy,* vol. 6, no. 2, pp. 022001, 2016.

[28] M. Mehrabian, S. Dalir, G. Mahmoudi, B. Miroslaw, M. G. Babashkina, A. V. Dektereva, and D. A. Safin, "A Highly Stable All-Inorganic CsPbBr3 Perovskite Solar Cell," *European Journal of Inorganic Chemistry,* vol. 2019, no. 32, pp. 3699-3703, 2019.

[29] S. Yun, Y. Qin, A. R. Uhl, N. Vlachopoulos, M. Yin, D. Li, X. Han, and A. Hagfeldt, "New-generation integrated devices based on dye-sensitized and perovskite solar cells," *Energy & Environmental Science,* vol. 11, no. 3, pp. 476-526, 2018.

[30] S.-M. Yoo, S. J. Yoon, J. A. Anta, H. J. Lee, P. P. Boix, and I. Mora-Sero, "An equivalent circuit for perovskite solar cell bridging sensitized to thin film architectures," *Joule,* vol. 3, no. 10, pp. 2535-2549, 2019.

[31] C. C. Katsidis, and D. I. Siapkas, "General transfer-matrix method for optical multilayer systems with coherent, partially coherent, and incoherent interference," *Applied optics,* vol. 41, no. 19, pp. 3978-3987, 2002.

[32] S. O. A. a. M. M. Hassan, "DSSC optical modelling using characterization matrix method ", 2020.

[33] B. M. Soucase, I. Guaita Pradas, and K. R. Adhikari, "Numerical Simulations on Perovskite Photovoltaic Devices," 2016.

[34] F. S. Jahantigh, Mohammad Javad, "The effect of HTM on the performance of solid-state dye-sanitized solar cells (SDSSCs): a SCAPS-1D simulation study," *Applied Physics A,* vol. 125, no. 4, 2019.

[35] M. Mehrabian, and S. Dalir, "Numerical simulation of highly efficient dye sensitized solar cell by replacing the liquid electrolyte with a semiconductor solid layer," *Optik,* vol. 169, pp. 214-223, 2018.

[36] G. B. Kazeem Abdullahi Ojotu, "Simulation of an Optimized Poly 3-Hexylthiophene (P3HT) based solid state Dye Sensitized Solar Cell (ss-DSSC) using SCAPS," *International Journal of Modern Research in Engineering and Technology (IJMRET),* vol. 5, no. 2, 2020.

[37] N. P. Bansal, and R. H. Doremus, *Handbook of glass properties*: Elsevier, 2013.

[38] P. Wen, Y. Han, and W. Zhao, "Influence of TiO$_2$ Nanocrystals Fabricating Dye-Sensitized Solar Cell on the Absorption Spectra of N719 Sensitizer," *International Journal of Photoenergy,* vol. 2012, pp. 906198, 2012/07/08, 2012.

[39] A. D. Rakić, A. B. Djurišić, J. M. Elazar, and M. L. Majewski, "Optical properties of metallic films for vertical-cavity optoelectronic devices," *Applied optics,* vol. 37, no. 22, pp. 5271-5283, 1998.

[40] G. Haidari, "Comparative 1D optoelectrical simulation of the perovskite solar cell," *AIP Advances,* vol. 9, no. 8, pp. 085028, 2019.

[41] A. A. Eid, Z. S. Ismail, and S. O. Abdellatif, "Optimizing SCAPS model for perovskite solar cell equivalent circuit with utilizing Matlab-based parasitic resistance estimator algorithm." pp. 503-507.

[42] S. V. V. Usha Mandadapu, K. Thyagarajan, "Numerical Simulation of Ch3Nh3PbI3-XClx Perovskite solar cell using SCAPS-1D," *International Journal of Engineering Science Invention*, pp. 40-45, 2017.

[43] D. Liu, Z. Hu, W. Hu, P. Wangyang, K. Yu, M. Wen, Z. Zu, J. Liu, M. Wang, W. Chen, M. Zhou, X. Tang, and Z. Zang, "Two-step method for preparing all-inorganic CsPbBr3 perovskite film and its photoelectric detection application," *Materials Letters,* vol. 186, pp. 243-246, 2017.

[44] X. Li, Y. Tan, H. Lai, S. Li, Y. Chen, S. Li, P. Xu, and J. Yang, "All-Inorganic CsPbBr3 Perovskite Solar Cells with 10.45% Efficiency by Evaporation-Assisted Deposition and Setting Intermediate Energy Levels," *ACS Appl Mater Interfaces,* vol. 11, no. 33, pp. 29746-29752, Aug 21, 2019.

[45] H. Yuan, Y. Zhao, J. Duan, Y. Wang, X. Yang, and Q. Tang, "All-inorganic CsPbBr3 perovskite solar cell with 10.26% efficiency by spectra engineering," *Journal of Materials Chemistry A,* vol. 6, no. 47, pp. 24324-24329, 2018.

[46] M. M. Hassan, A. Sahbel, S. O. Abdellatif, K. A. Kirah, and H. A. Ghali, "Toward low-cost, stable, and uniform high-power LED array for solar cells characterization." p. 114960Q.

[47] M. Hassan, N. Iskander, S. Abdellatif, K. Kirah, and H. Ghali, *Investigating parasitic resistance of mesoporous-based solar cells with respect to thin-film and conventional solar cells*, p.^pp. OPP: SPIE, 2020.